Chemosphere 366 (2024) 143532

Contents lists available at ScienceDirect

Chemosphere

journal homepage: www.elsevier.com/locate/chemosphere

Bismuth oxyiodide-based composites for advanced visible-light activation of peroxymonosulfate in pharmaceutical mineralization

Laura Huidobro [a,b], Anna Domingo [a], Elvira Gómez [a,b], Albert Serrà [a,b,*]

[a] Grup d'Electrodeposició de Capes Primes i Nanoestructures (GE-CPN), Departament de Ciència de Materials i Química Física, Universitat de Barcelona, Martí i Franquès, 1, E-08028, Barcelona, Catalonia, Spain
[b] Institute of Nanoscience and Nanotechnology (IN^{2}UB), Universitat de Barcelona, Barcelona, Catalonia, Spain

HIGHLIGHTS

- Solvothermal BiOI yield microspheres, while electrodeposition flower-like structures.
- $BaFe_{12}O_{19}$ nanoparticles in BiOI and Bi_5O_7I enhanced photocatalytic performance.
- Bi_5O_7I (ED)-BFO composite showed highest degradation and mineralization efficiency.
- Composites are stable and reusable 15 cycles for water pollutant degradation.

GRAPHICAL ABSTRACT

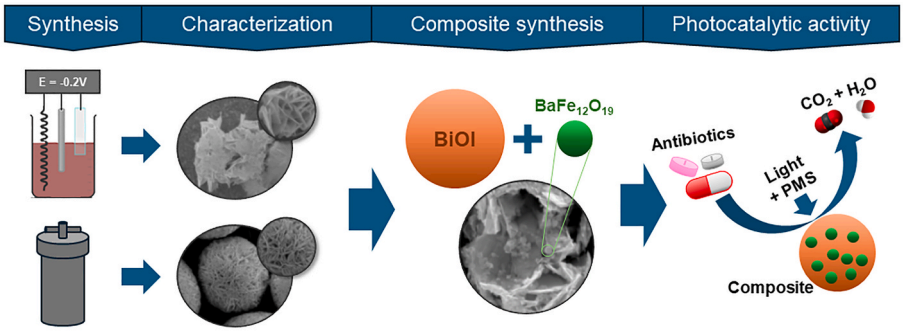

ARTICLE INFO

Handling Editor: S Garcia-Segura

Keywords:
Bismuth oxyiodides
Barium ferrite
Peroxymonosulfate
Advanced oxidation processes
Visible-light photocatalysis
Pharmaceutical pollutants

ABSTRACT

The presence of pharmaceutical pollutants in water bodies represents a significant environmental and public health concern, largely due to their inherent persistence and potential to induce antibiotic resistance. Advanced oxidation processes (AOPs) that employ peroxymonosulfate (PMS) activation have emerged as an effective means of degrading these contaminants. Bismuth oxyiodides (BiOI), which are known for their visible-light photocatalytic properties, demonstrate considerable potential for removal of pharmaceutical pollutants. This study examines the synthesis and performance of BiOI-based composites with barium ferrite (BFO) nanoparticles for enhanced PMS activation under visible light. BiOI and Bi_5O_7I were synthesized via solvothermal and electrodeposition methods, respectively, and their morphologies and crystalline structures were observed to exhibit distinctive characteristics following annealing. The formation of the composite with BFO resulted in an improvement in the catalytic properties, which in turn enhanced the surface area and availability of active sites. The objective of the photocatalytic studies was to evaluate the degradation and mineralization of tetracycline (TC) under visible light, PMS, and combined conditions. The Bi_5O_7I(ED)-BFO catalyst was identified as the optimal candidate, achieving up to 99.8% TC degradation and 99.4% mineralization within 90 min at room temperature. The synergistic effect of BFO in BiOI-based composites significantly enhanced performance across all conditions, indicating their potential for efficient remediation of pharmaceutical pollutant. The material's performance was further evaluated in tap water, where the degradation efficiency decreased to 56.4% and

* Corresponding author. Grup d'Electrodeposició de Capes Primes i Nanoestructures (GE-CPN), Departament de Ciència de Materials i Química Física, Universitat de Barcelona, Martí i Franquès, 1, E-08028, Barcelona, Catalonia, Spain.
E-mail address: a.serra@ub.edu (A. Serrà).

https://doi.org/10.1016/j.chemosphere.2024.143532
Received 26 July 2024; Received in revised form 25 September 2024; Accepted 11 October 2024
Available online 12 October 2024

mineralization to 38.2%. These results reflect the challenges posed by complex water matrices. However, doubling the PMS concentration to 5 mM led to improved outcomes, with 93.8% degradation and 81.4% mineralization achieved. These findings demonstrate the material's robust potential for treating pharmaceutical pollutants in real-world conditions, advancing sustainable water treatment technologies.

1. Introduction

Antibiotic pollution represents a significant global concern due to the long-lasting effects of these substances in aquatic ecosystems, even at minimal concentrations. This persistence presents a significant threat to aquatic species and human health, as it facilitates the proliferation of antibiotic-resistant bacteria. The principal means by which antibiotics enter into the environment is through the excretion of unmetabolized drugs in urine and feces (Felisardo et al., 2023; Roberts and Zembower, 2021; J. Wang et al., 2021; Yuan et al., 2023). Furthermore, the issue is exacerbated by the frequent use of antibiotics in human medicine and intensive livestock farming, where large populations of animals in confined spaces are regularly administered antibiotics (Felisardo et al., 2023; Robins et al., 2024; J. Wang et al., 2021).

The conventional methods of removal of these drugs, such as biological degradation, chemical oxidation, absorption, electrochemical processes, and filtration, are inadequate for the removal of drugs at very low concentrations. In response, advanced oxidation processes (AOPs) have emerged as a promising solution. AOPs encompass a range of treatment methods, including photocatalysis, the Fenton process, sulfate radical-based oxidation (SR-AOPs), ozone-based techniques, sonocatalysis, and electrocatalysis (Brillas, 2022; Kanakaraju et al., 2018; Lima et al., 2019; Paragas et al., 2021; Wang and Wang, 2020). These processes generate highly reactive radicals that decompose and mineralize organic compounds into harmless byproducts, including water and carbon dioxide. This approach is economically viable, accessible, straightforward, cost-effective, and environmentally friendly, rendering it suitable for both resource-limited and developed countries (Kanakaraju et al., 2018; Lima et al., 2019; Miklos et al., 2018).

Bismuth oxyhalides, in particular bismuth oxyiodides, have generated considerable attention due to their photocatalytic properties. They display excellent responsiveness to visible light and enhance catalytic reactions under solar irradiation (Arumugam et al., 2021; Huidobro et al., 2024; Li et al., 2024; Tekin et al., 2023; L. Wang et al., 2021). BiOI represents a notable example of this phenomenon, exhibiting the characteristics of a p-type semiconductor with the smallest band gap energy among bismuth oxyhalides. The layered structure of BiOI allows for the efficient separation of electron-hole pairs during photocatalysis. Upon exposure to light, BiOI generates electron-hole pairs in its valence and conduction bands, which interact with oxygen and water to produce radical anions such as superoxide (Huidobro et al., 2024; R. MD Matiur et al., 2021; Tekin et al., 2023; L. Wang et al., 2021).

In contrast, other bismuth oxyhalides, such as Bi_5O_7I, have the potential for wastewater treatment due to their ability to form hydroxyl radicals under visible light as the oxidation potential of the valence band increases with the iodine vacancies (Huidobro et al., 2024; Liu and Wang, 2016; R. Md Matiur et al., 2021; R. MD Matiur et al., 2021; Putri et al., 2019). Thermal treatment results in alterations to the crystalline structure of BiOI, which in turn affects the uniformity and morphology of the material. It has been demonstrated that the replacement of iodine atoms with oxygen atoms increases the band gap energy of these compounds, resulting in the formation of Bi_5O_7I or $Bi_7O_9I_3$, depending on the annealing conditions. These variations in atomic composition exert a profound influence on structural defects, band energy, and recombination effects (Huidobro et al., 2024; Liu and Wang, 2016; R. Md Matiur et al., 2021; R. MD Matiur et al., 2021; Putri et al., 2019).

Notwithstanding the observed enhancements in the reduction of recombination through the formation of Bi_5O_7I or $Bi_7O_9I_3$ species, significant challenges remain in extending the lifetime of photo-generated charge carriers in bismuth oxyiodides. The current research agenda is focused on enhancing these materials through the incorporation of metals, non-metals, noble metals, and semiconductor compounds. These efforts are focused on mitigating of recombination processes and enhancing the overall efficiency of bismuth oxyiodides in photocatalytic applications (Huidobro et al., 2024; Liu and Wang, 2016; R. Md Matiur et al., 2021; R. MD Matiur et al., 2021; Putri et al., 2019).

In addition to enhancing the photocatalytic activity of bismuth oxyiodides, they have demonstrated efficacy as catalysts for the activation of peroxymonosulfate (PMS) to produce sulfate radicals. These radicals possess a high redox potential (2.6–3.1 V), which enables them to oxidize a diverse range of organic pollutants. In comparison to hydroxyl radicals, sulfate radicals exhibit a longer lifespan (30–40 μs) and are effective over a broader pH range (Cao et al., 2022; Pang et al., 2021; Shang et al., 2023; Wacławek et al., 2017). The activation of PMS without the use of catalysts resulted in the inefficient decomposition of the persulfate anion ($S_2O_8^{2-}$), with only modest effects observed when PMS was used alone. A variety of techniques have been developed to activate PMS, including thermal decomposition, ultrasonic treatment, ultraviolet irradiation, alkaline activation, laser activation, and transition metal catalysis (Bein et al., 2023; Bujaldón et al., 2024; Guo et al., 2020; Hjiri et al., 2024; Serrà et al., 2024). The prominence of SR-AOPs can be attributed to their effectiveness across different pH levels, higher oxidizing potential, and reduced sensitivity to operating conditions. PMS functions as a powerful oxidizing agent in water treatment, generating sulfate radicals ($SO_4^{\bullet-}$) that facilitate the degradation and mineralization of organic contaminants. This capacity helps to overcome challenges such as electron-hole recombination inherent in multiple photocatalytic processes (Lim and Hoffmann, 2020; Serrà et al., 2024; Wang and Wang, 2018).

Recently, barium ferrite ($BaFe_{12}O_{19}$) has emerged as a promising candidate for the activation of PMS. $BaFe_{12}O_{19}$ displays intrinsic catalytic activity for the generation sulfate radicals and exhibits magnetic properties that are conductive to the facilitation of separation and recovery processes subsequent to PMS activation. The stability and durability of this material under various environmental conditions make it suitable for long-term applications in water treatment. Furthermore, its cost-effectiveness enhances its suitability for such applications (Ashraf et al., 2024; Bayantong et al., 2021; Hjiri et al., 2024; Wang et al., 2024; Xu et al., 2019).

The search for photocatalysts with the versatility to effectively eliminate a wide range of organic contaminants in aquatic environments remains a critical challenge. This study examines the synthesis of bismuth oxyiodides through electrodeposition and solvothermal methods, with an analysis of their compositional and structural characteristics to identify the most effective synthesis techniques. Once the optimal synthesis method has been identified, the research will focus on enhancing the photocatalytic properties of the material by synthesizing composites with added barium ferrite nanoparticles. This study examines the efficiency of bismuth oxyiodides-barium ferrite composites in the degradation and mineralization of contaminants in single- and multipollutant solutions under visible light irradiation. The use of bismuth oxyiodide-based composites for the visible-light activation of peroxymonosulfate represents a pioneering advancement in this field. This approach exploits the efficiency and sustainability of AOPs to address the pressing issue of pharmaceutical pollution mitigation. In conclusion, the objective of this research is to enhance environmental quality and human health outcomes.

2. Experimental section

2.1. Synthesis and characterization of bismuth oxyiodides-barium ferrite composites

In this study, composites of BiOI and Bi_5O_7I–$BaFe_{12}O_{19}$ were fabricated. BiOI, which serves also as the base material for synthesizing Bi_5O_7I, was prepared using two readily scalable processes:

- **Solvothermal synthesis (ST):** In order to prepare BiOI using the solvothermal method (referred to as BiOI ST), two solutions were prepared (Lee et al., 2016; Mera et al., 2017; Qin et al., 2013; Wang et al., 2011; Xia et al., 2011a, 2011b). The starting materials, Bi $(NO_3)_3{\cdot}5H_2O$ (≥98% purity, Sigma-Aldrich) and KI (≥99% purity, Panreac), were separately dissolved in 50 mL of ethylene glycol (EG, 99.8% purity, Sigma-Aldrich). Subsequently, the KI solution was added to the $Bi(NO_3)_3$ solution at a slow rate, while maintaining stirring. The resulting solution was then stirred and sonicated for a period of 10 min each, until a homogeneous and stable mixture was achieved. Subsequently, the solution was transferred into a Teflon-lined stainless-steel autoclave. Subsequently, the solvothermal treatment was conducted at 160 °C for a period of 6 h, after which the temperature was reduced to room temperature. The nanoparticles of BiOI were obtained as a powder at the bottom of the autoclave. Subsequently, the synthesized BiOI powder was washed repeatedly with Milli-Q water and ethanol (EtOH, Panreac, 96%) in order to completely remove the ethylene glycol. The washed powder was then filtered and dried at 120 °C for 12 h. To prepare Bi_5O_7I, the BiOI nanoparticles were annealed in an air atmosphere at 420 °C for 4 h. The temperature was increased gradually at a rate of 2 °C per minute from 20 °C, and then cooled down using the same decreasing slope.
- **Electrosynthesis (ED):** The BiOI thin films were synthesized using an electrodeposition method previously detailed in a study (Huidobro et al., 2024), employing a three-electrode cell system. The electrochemical bath consisted of 29 mM $Bi(NO_3)_3$, 289 mM KI, and a 41 mM p-benzoquinone solution in a 50:20 (V:V) H_2O solvent ratio. The electrodeposition process was conducted potentiostatically at a potential of −0.20 V (vs. Ag/AgCl). To detach the deposited film from the FTO substrate, an 8 mg mL^{-1} polyvinyl alcohol (PVA, Alfa Aesar, 98–99% hydrolyzed) solution was prepared using hot (90 °C) Milli-Q water, with the addition of ultrasound and vigorous stirring to ensure a homogeneous transparent solution. Subsequently, the PVA solution was applied to the films, ensuring complete coverage of the deposited surface. Subsequently, the samples were dried on a heating plate at temperatures between 40 and 55 °C for a period of 2 h. Thereafter, the polymer-BiOI layer was carefully peeled off and collected. Subsequently, the samples were rinsed in hot Milli-Q water and washed repeatedly with Milli-Q water and ethanol in order to remove any residual PVA. The resulting BiOI-based material was then dried and collected as a powder. To synthesize Bi_5O_7I, the BiOI powder was subjected to annealing in an air atmosphere at 420 °C for a period of 4 h. The temperature was increased gradually at a rate of 2 °C per minute from 20 °C and then cooled down using the same decreasing slope.

To prepare BiOI/$BaFe_{12}O_{19}$ and Bi_5O_7I/$BaFe_{12}O_{19}$ composites, solvothermal (ST) and electrodeposition (ED) methods were employed. A 1 wt% weight content of $BaFe_{12}O_{19}$ nanopowder (Aldrich, BET <100 nm, >97%) was introduced into moderate Milli-Q water and sonicated for 30 min, followed by stirring for 16 h to obtain a homogeneous composite suspension. Finally, the suspension was washed with water and ethanol, centrifuged, and dried to obtain the nanocomposite powder.

The surface morphology and architecture were analyzed using a field emission scanning electron microscope (FE-SEM, JEOL J7100) equipped with an energy-dispersive X-ray spectroscopy (EDX) detector in order to determine the elemental composition of the samples. The effective surface area of the materials was quantified utilizing adsorption-desorption isotherms with nitrogen at 77 K (Micromeritics TriStar Surface Area and Porosity Analyzer) following degassing with a BacPrep 061 Sample Degas System. The surface area was determined by the Brunauer-Emmett-Teller (BET) method. X-ray photoelectron spectroscopy (XPS, PHI Quantera SXM) was employed to analyze the chemical composition. This entailed the utilization of monochromated Al K_α X-rays with a 200 μm spot size in ultra-high vacuum. The electrons ejected from the source were collected at an emission angle of 45° and directed to a hemispherical capacitor analyzer in fixed analyzer transmission mode. The measurements were assisted by the use of an active low-voltage ion gun and an electron neutralizer. The spectrometer was calibrated in accordance with ISO 15472:2010 standards using etched, clean surfaces of pure copper, silver, and gold in order to maintain an accuracy of within 0.2V. The survey spectra were recorded with a pass energy of 280 eV and a step size of 1 eV, while the high-resolution spectra were captured at a pass energy of 55 eV with a step size of 0.05 eV. The crystalline structure of the samples was determined using X-ray diffraction (XRD) with a PANalytical X'Pert PRO MPD alpha1 powder diffractometer in Bragg-Brentano θ-2θ geometry, with a radius of 240 mm. The scanning range was 4.5–100°, with a measurement time of 200 s and a step size of 0.026°. The optoelectronic properties of the prepared materials were characterized by UV–visible diffuse reflectance spectra, which were obtained using a PerkinElmer Lambda 900 UV spectrophotometer.

2.2. Study of degradation and mineralization of organic pollutants

A systematic study was conducted to investigate the degradation and mineralization of tetracycline (TC) using BiOI-based materials and their composites under a range of conditions. These included visible light irradiation, the presence of PMS, and a combination of both. Each photocatalyst was tested independently in triplicate. In each test, 5 mg of photocatalyst was introduced into 10 mL of TC solution (20 ppm). For the PMS experiments, 150 μL of a 167 mM solution was added to achieve a 2.5 mM PMS concentration. Visible light irradiation was applied using a 1.6 W white light-emitting diode (LED) strip ($2.2{\cdot}10^{-3}$ W cm^{-2}). Prior to commencing the catalytic study, the sample was maintained in the dark for a period of over 30 min in order to achieve equilibrium between adsorption and desorption. Subsequently, PMS was added (if applicable) and/or the sample was irradiated. The absorbance was measured with a UV–vis spectrophotometer (Shimadzu UV-1800) at different intervals over 90 min, with the photocatalyst removed by centrifugation to avoid interference.

The total organic carbon (TOC) content was determined by high-temperature combustion analysis (TOC-VCSH, Shimadzu) in order to analyze mineralization. Additionally, independent experiments were conducted to assess the impact of $BaFe_{12}O_{19}$ on the degradation and mineralization processes in the absence of BiOI. In order to ascertain the most effective catalysts and conditions, reusability and stability were evaluated by repeating the photocatalytic degradation process for 15 cycles under the same conditions. The efficiency of TC degradation was quantified at the conclusion of each cycle. The total amount of bismuth, barium, and iron ions dissolved during the process was determined in order to analyze the (photo)chemical stability of the catalyst using inductively coupled plasma optical emission spectroscopy (ICP-OES, Optima 8300 PerkinElmer instrument). Furthermore, FE-SEM and XRD analyzes were conducted on the catalysts after the 15th cycle to assess the durability of the composites.

In order to gain insight into the photocatalytic mechanism, radical trapping experiments were conducted utilizing specific scavengers. The following scavengers were used to trap the specific radicals: 1 mM benzoquinone (BQ) for superoxide radicals ($O_2^{\bullet-}$), 1 mM methanol (MeOH) for hydroxyl ($^{\bullet}OH$) and sulfate ($SO_4^{\bullet-}$) radicals, 1 mM *tert*-butyl alcohol (TBA) for hydroxyl radicals ($^{\bullet}OH$), and 1 mM ethylenediamine tetraacetic acid disodium salt (EDTA) for photogenerated holes (h^+).

These experiments enabled the identification of the active radical species generated (Lv et al., 2024; Meng et al., 2024; Qi et al., 2016; Zhang et al., 2024).

The consumption of PMS during the irradiation process was quantified using iodometry. In a typical experiment, 10 mL of the reaction medium and 2.5 mM of PM were exposed to the catalyst under both dark and light conditions for 90 min. Subsequently, the supernatant was combined with 3.4 g of potassium iodide (KI, Sigma-Aldrich, >99.0%) and agitated magnetically for 30 min. This allowed for the reaction of PMS with iodide ions, resulting in the formation of triiodide ions, whose concentration was monitored through the use of UV–vis spectroscopy, with measurements taken at the absorption peak at 352 nm. The intensity of the peak was found to be directly proportional to the concentration of non-activated PMS.

To assess the concentration of sulfate and hydroxyl radicals, a sensitive spectrophotometric method was employed. The relative concentration of sulfate radicals was indirectly determined by measuring the formation of Ce(IV) through UV–vis spectrophotometry, following the reaction of sulfate radicals with Ce(III). In these experiments, the catalyst was immersed in a solution containing 10 mM $Ce_2(SO_4)_3$ and 2.5 mM PMS at a pH of 7.0. The absorbance of Ce(IV) at 320 nm was recorded at various time points over a 90-min period in both dark and light-irradiated conditions. The concentration of sulfate radicals was calculated using a calibration curve based on known Ce(IV) sulfate concentrations.

The concentration of hydroxyl radicals was quantified by monitoring the time-dependent decrease in the fluorescence intensity of fluorescein sodium salt (Sigma-Aldrich). A solution containing 8 μM fluorescein sodium salt (excitation at 303 nm, emission at 515 nm) was prepared and the catalyst was immersed in 10 mL of this solution, both in the absence and presence of 2.5 mM PMS, at pH 7.0. The experiments were also conducted in the absence and presence of light. To ascertain the concentration of fluorescein sodium salt, a calibration curve was constructed by comparing the fluorescence values to those of standard solutions with known concentrations. Fluorescence spectra were recorded using an AMINCO-Bowman Series 2 spectrofluorometer with a quartz microcell at a temperature of 25 °C. Following the characterization of all materials and the analysis of their degradation and mineralization efficiencies, the most effective catalyst was selected for the degradation of multi-pollutant solutions. Table 1 presents the composition of these solutions, which include pharmaceuticals such as tetracycline (TC) and levofloxacin (LEV) and dyes such as methylene blue (MB) and rhodamine B (Rh–B).

TOC measurements were taken for each solution after 90 and 180 min of visible light exposure in the presence of 2.5 mM PMS (Solution 1) and 10 mM PMS (Solution 2). The reusability of the catalyst was tested with 20 ppm and 80 ppm multi-pollutant solutions over 15 cycles. After these tests, the morphological, structural, and compositional characteristics of the catalyst were analyzed. The presence of bismuth, iron, and barium ions in the solution was quantified to assess the integrity of the catalyst using inductively coupled plasma optical emission spectroscopy (ICP-OES, Optima 8300 PerkinElmer instrument).

To illustrate the potential of the process in a realistic context, tap water was collected from the Chemistry School at the University of Barcelona, filtered through a 0.5-μm filter, and subsequently employed. The water exhibited moderate buffering, with an alkalinity of 166 mg $CaCO_3$ L^{-1} and a pH of 7.75, which was slightly basic. The water was moderately hard, with a total hardness of 234 mg $CaCO_3$ L^{-1}, primarily derived from calcium (67.2 mg L^{-1}) and magnesium (16.6 mg L^{-1}). The principal mineral constituents were sodium (106 mg L^{-1}), chloride (175 mg L^{-1}), sulfate (79.6 mg L^{-1}), and a TOC of 4.9 ppm. In order to conduct the experiment, 20 ppm of TC was added to the water, and the pH was adjusted to 7.00. The most effective catalyst was immersed in contaminated tap water for 60-min period in the absence of light. PMS was introduced to reach a concentration of 2.5 or 5.0 mM, and the degradation of TC and organic matter mineralization was monitored via UV–vis spectroscopy and TOC analysis under light irradiation for 90 min.

Table 1
Composition of multicomponent solutions.

Solution	Concentration/ppm					pH
	Total	TC	LEV	MB	Rh–B	
(1)	20	5	5	5	5	7
(2)	80	20	20	20	20	7

3. Results and discussion

3.1. Synthesis and characterization of bismuth oxyiodides-barium ferrite composites

The synthesis of BiOI was achieved via solvothermal synthesis and electrodeposition, both of which are suitable for the scalable production of photocatalysts. The resulting powder was identified as BiOI, exhibiting an orange coloration (Hu et al., 2014; Huidobro et al., 2024; Mera et al., 2017; Shi et al., 2012; Xia et al., 2011a). In the course of this study, the BiOI prepared via solvothermal synthesis is designated as BiOI (ST), whereas that prepared via electrodeposition is labelled as BiOI (ED). Subsequently, both BiOI (ST) and BiOI (ED) powders were subjected to annealing in air at 420 °C for 4 h, resulting in the production of Bi_5O_7I. Depending on its origin, Bi_5O_7I is referred to as either Bi_5O_7I (ST) or Bi_5O_7I (ED). The resulting Bi_5O_7I powder exhibited a pale-yellow coloration in both instances. Despite the similar color, the morphology of the two types of material differs significantly based on the synthesis process.

The synthesis of BiOI (ST) via the solvothermal method resulted in the formation of distinctive morphology with well-defined regular microspheres ranging from 4 to 6 μm (Fig. 1a). These microspheres were composed of numerous curved nanosheets and facets, which significantly enhanced the surface area and provided numerous active sites for reaction with pollutant molecules. In contrast, BiOI (ED) obtained through electrodeposition displayed a heterogeneous flower-like morphology with irregular curved nanosheets and fragments of 2.5–3.5 μm after detachment from the FTO substrate (Fig. 1b). Annealing affected the morphology of the Bi-based particles. Bi_5O_7I (ST) maintained particle size but exhibited a more compact structure with smaller, irregular curved nanosheets (Fig. 1c). Bi_5O_7I (ED), however, developed a fluffier and spongier architecture (Fig. 1d).

The BET surface area measurements were found to be in accordance with the observed FE-SEM morphologies (Fig. 2a). The surface area of BiOI (ST) was determined to be 32.0 m^2g^{-1}, while that of BiOI (ED) was found to be 52.5 m^2g^{-1}. Following annealing, the surface area of Bi_5O_7I (ST) decreased significantly, reaching 7.2 m^2g^{-1}. This resulted in the formation of compact, almost perfect spheres with small, thin, irregular, curved nanosheets. The Bi_5O_7I (ED) sample retained a spongier and more amorphous structure with a surface area of 33.6 m^2g^{-1}.

Fig. 2b illustrates the diffractogram patterns of the prepared materials. The diffractograms of the prepared materials reveal the presence of BiOI (JCPDS No. 00-010-0445) and Bi_5O_7I (JCPDS No. 00-040-0548). The Bi_5O_7I samples exhibited residual BiOI peaks, which may be attributed to the presence of residual impurities remaining after thermal treatment. For BiOI (ST), significant reflection planes were identified at $2\theta = 29.4°$, 31.7°, 45.5°, and 55.3°, corresponding to the (102), (110), (200), and (212) crystalline planes, respectively. The BiOI (ED) displayed comparable crystalline patterns to those observed in BiOI (ST), aligning well with the tetragonal phase of BiOI, as documented in the standard reference card. The Bi_5O_7I exhibited an orthorhombic structure with main reflection angles at approximately $2\theta = 28°$, 31°, 33°, 45.9°, 53°, and 55.5°, corresponding to the (312), (004), (204), (204), (316), and (912) planes. These findings substantiate the high degree of

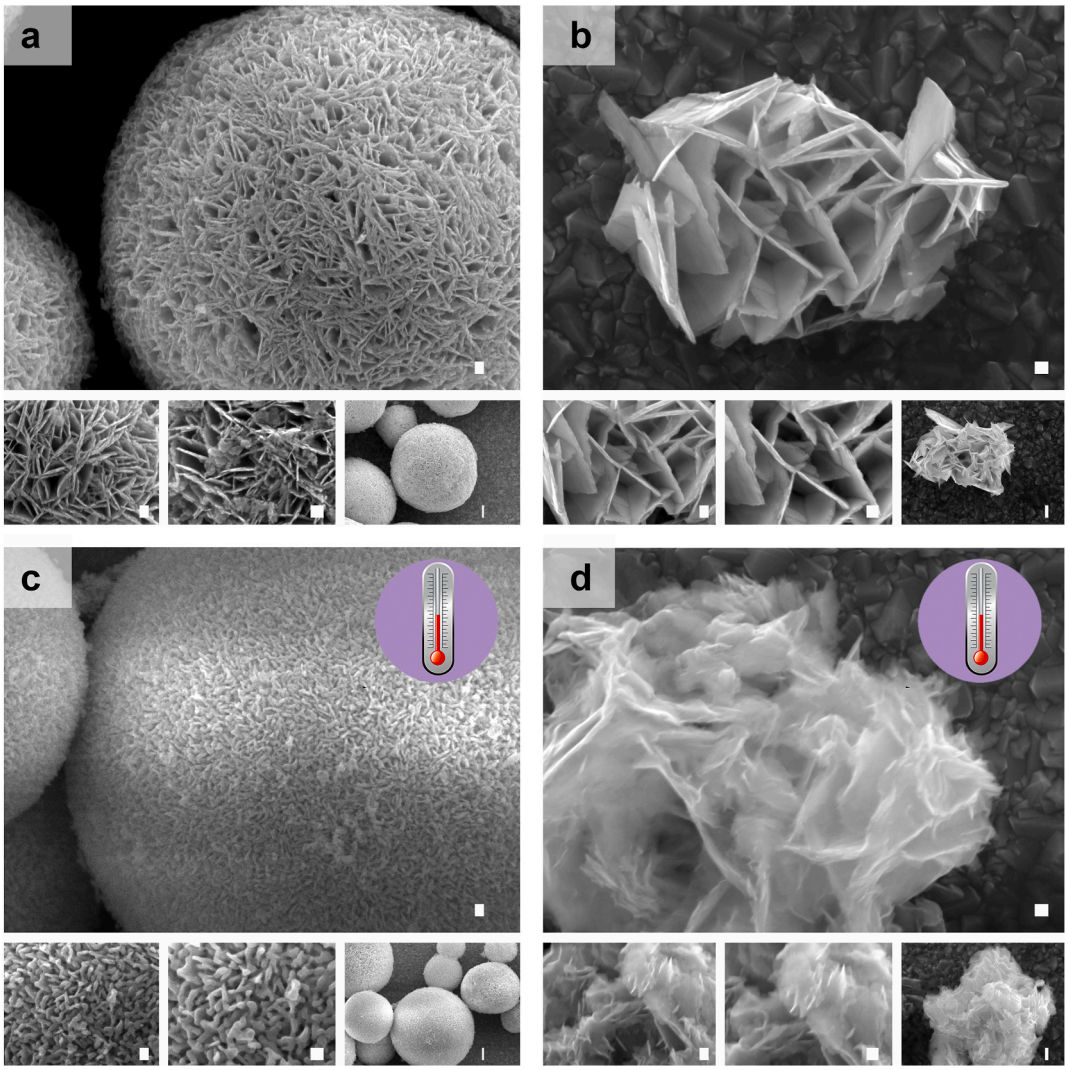

Fig. 1. FE-SEM micrographs of (a) BiOI (ST), (b) BiOI (ED), (c) Bi_5O_7I (ST), and (d) Bi_5O_7I (ED). Scale bar: 100 nm.

crystallinity observed in both BiOI and Bi_5O_7I materials, with no discernible contamination by impurities.

The XPS analysis of the Bi 4f, I 3d, and O 1s spectra for BiOI-based materials examined the chemical nature of the catalysts (Fig. 2c). The C 1s peak at 284.8 eV was employed as a reference point. Both BiOI (ED) and BiOI (ST) exhibited Bi 4f peaks at 159.2–159.3 eV and 164.5–164.6 eV, respectively. These peaks correspond to the Bi^{3+} $4f_{7/2}$ and Bi^{3+} $4f_{5/2}$ signals of the Bi–O bond, indicating that bismuth was present in the +3-oxidation state. Additionally, minor peaks at 157.2 eV and 162.5 eV were also observed, corresponding to Bi-metal bonds, which indicate the presence of a small amount of Bi(0). Following the thermal treatment, the intensity of these peaks decreased, thereby confirming the presence of bismuth in the +3 oxidation state in Bi_5O_7I.

The I 3d spectra for all samples showed peaks at 619.1–619.2 eV and 630.5–630.6 eV, which were attributed to I $3d_{5/2}$ and I $3d_{3/2}$, respectively. This confirmed the presence of iodide ions in BiOI and Bi_5O_7I structures. The O 1s spectra of BiOI (ST) and Bi_5O_7I (ST) showed an asymmetric peak at 529.7 eV, indicative of lattice oxygen in Bi–O bonds, with a shoulder peak at 531.3 eV, likely from hydroxyl groups or adsorbed water. In the case of electrodeposited samples, the presence of a peak at 532.8 eV indicates the possibility of exposure to moisture or residual organic species resulting from the detachment of PVA. The XPS results corroborate the successful synthesis of BiOI and Bi_5O_7I, thereby validating their composition and structure through the observed binding energies, which were consistent with their chemical environments.

The combination of different types of BiOI-based particles with varying concentrations of magnetic ferrites has resulted in the expansion of the range of useful photocatalysts. The efficacy of $BaFe_{12}O_{19}$ concentrations ranging from 1 wt% to 10 wt% was evaluated. The 1 wt% concentration was identified as the most effective, yielding a homogeneous composite that could be collected externally via magnetic actuation. Higher concentrations resulted in the formation of mixtures comprising both composite and free $BaFe_{12}O_{19}$ nanoparticles. The supporting information provides detailed structural, textural, morphological, and chemical characterization of $BaFe_{12}O_{19}$. The composites prepared with BiOI (ST or ED) and Bi_5O_7I (ST or ED) are designated as follows: BiOI (ST)-BFO, BiOI (ED)-BFO, Bi_5O_7I (ST)-BFO, and Bi_5O_7I (ED)-BFO.

As illustrated in Fig. 3, the images exhibited a sophisticated microstructure with discernible characteristics. In all cases, the morphology exhibited a resemblance to that of the BiOI or Bi_5O_7I base, albeit with a diminished degree of definition. It was partially coated with barium ferrite nanoparticles. The distribution of barium ferrite on the bismuth oxyiodide was observed to be relatively uniform, although notable accumulations were evident in select regions. Additionally, the images indicated robust interfacial interactions between the barium ferrite and BiOI phases, suggesting strong adhesion and potential synergistic effects. Moreover, the incorporation of $BaFe_{12}O_{19}$ was observed to

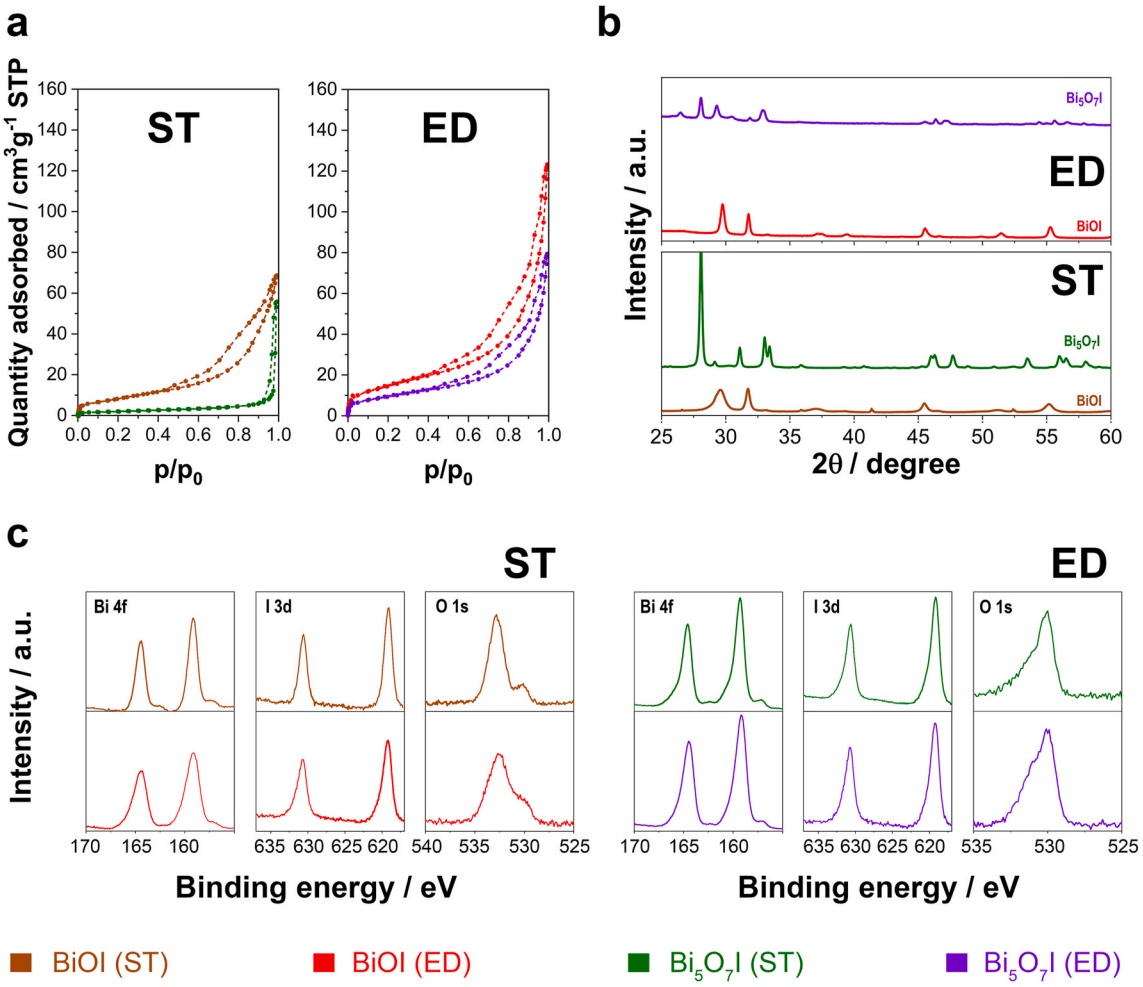

Fig. 2. Characterization of BiOI-based materials: (a) Nitrogen adsorption-desorption isotherms, (b) X-ray diffraction (XRD) patterns, and (c) X-ray photoelectron spectroscopy (XPS) spectra for Bi 4f, I 3d, and O 1s.

augment the surface area of the composite, which is anticipated to optimize the catalytic performance.

The adsorption-desorption isotherms of the composites corroborated the findings of the FE-SEM analysis, demonstrating that the composites prepared with electrodeposited catalysts exhibited markedly elevated BET surface areas under identical pressure conditions compared to those prepared via the solvothermal method. Notably, the adsorption values for the electrodeposited catalysts reached 150 $cm^3\ g^{-1}$, whereas the solvothermal samples did not exceed 60 $cm^3\ g^{-1}$ (Fig. 4a). The data indicate that the composites with ED catalysts exhibited a higher surface area, suggesting a greater availability of active sites for photocatalysis and thus superior performance. The estimated surface areas were as follows: The BET surface areas of the BiOI (ST)-BFO, BiOI (ED)-BFO, Bi_5O_7I (ST)-BFO, and Bi_5O_7I (ED)-BFO composites were found to be 26.3, 66.5, 17.7, and 60.7 $m^2\ g^{-1}$, respectively. It is noteworthy that BiOI (ST)-BFO exhibited a smaller area than the BiOI (ST). This can be attributed to the partial covering of curved nanosheets and the lack of compensation by the integration of $BaFe_{12}O_{19}$ nanoparticles. In contrast, Bi_5O_7I (ST)-BFO exhibited a higher surface area than Bi_5O_7I (ST) due to the incorporation of $BaFe_{12}O_{19}$ nanoparticles, which increased the accessible surface area.

As illustrated in Fig. 4b, the crystal structure of the composites exhibited similarities to that of the non-magnetised compounds, as the ferrites were present in minute quantities, approximately 1%. However, the Bi_5O_7I (ST)-BFO exhibited low-intensity peaks indicating $BaFe_{12}O_{19}$ (JCPDS No. 01-084-0757) (marked in black in Fig. 4b), which were observed at $2\theta = 32.5°$, 35.8°, and 58°. These peaks correspond to the crystal lattice planes (107), (114), and (304), respectively. The diffraction pattern of Bi_5O_7I (ST)-BFO was less distinct due to the superposition of ferrite peaks. A low-intensity peak attributable to the untreated BiOI impurity was observed at $2\theta = 10.8°$, corresponding to the crystal plane (001) of BiOI (marked in blue). In the case of BiOI (ED)-BFO, the majority of the peaks observed were those of BiOI (ED), with the exception of a minor ferrite peak at $2\theta = 39.4°$, corresponding to the plane (205). In the diffraction pattern of Bi_5O_7I (ED)-BFO, peaks from potential BiOI (ED) impurities were observed (highlighted in green) at $2\theta = 9.5°$, 29.2°, and 31.8°, corresponding to (001), (102), and (110), as well as $BaFe_{12}O_{19}$ peaks at $2\theta = 30.4°$, 23.7°, 35.7°, and 57.5°, due to the crystal planes (110), (107), (114), and (304). The most prominent peaks, corresponding to the Bi_5O_7I structure (highlighted in purple), were observed at $2\theta = 28.0°$, 32.7°, 45.3°, 46.2°, 54.3°, and 55.5°, which correspond to the crystal planes (312), (204), (404), (024), (316), and (912), respectively. Fig. S1 illustrates the diffractogram for barium ferrites.

The XPS analysis examined the Bi 4f, I 3d, Ba 3d, Fe 2p, and O 1s spectra of the synthesized composites (Fig. 4c), utilizing the C 1s peak (284.8 eV) as a reference point. The Bi 4f spectra of the composites exhibited a correlation with those of the oxyiodides produced by both the ED and ST methods, displaying prominent peaks at 159.2–159.3 eV and 164.5–164.6 eV. These peaks correspond to the Bi^{3+} $4f_{7/2}$ and Bi^{3+} $4f_{5/2}$ states in the Bi–O bond of $[Bi_2O_2]^{2+}$. Minor peaks at 157.2 eV and 162.5 eV were identified as associated with the Bi-metal bond, indicating the presence of a minor amount of Bi(0). The I 3d spectra exhibited peaks at approximately 619.1–619.2 eV and 630.5–630.6 eV, thereby confirming the presence of iodide ions in BiOI and Bi_5O_7I. The

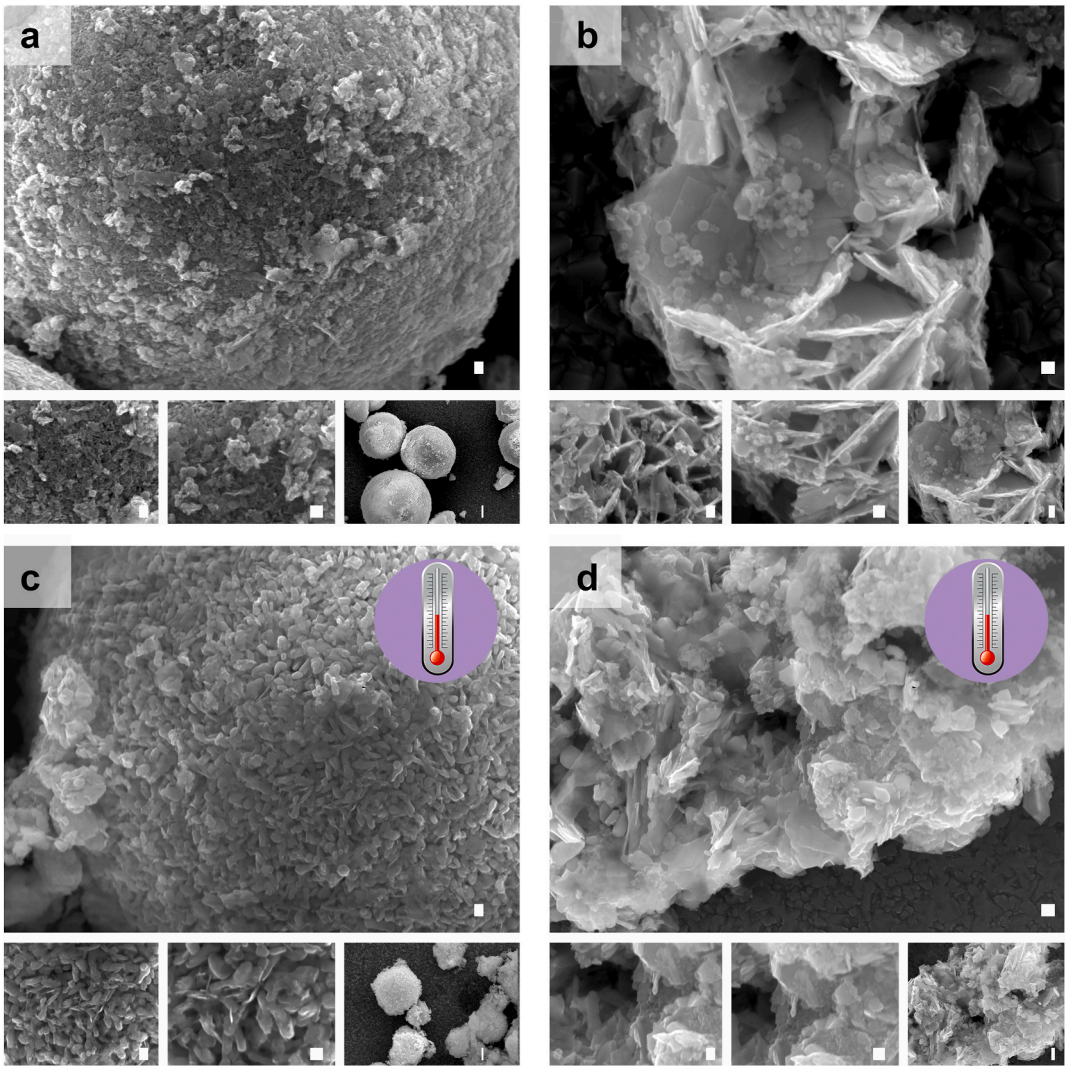

Fig. 3. FE-SEM micrographs of (a) BiOI (ST)-BFO, (b) BiOI (ED)-BFO, (c) Bi_5O_7I (ST)-BFO, and (d) Bi_5O_7I (ED)-BFO. Scale bar: 100 nm.

Ba 3d spectra exhibited peaks for Ba $3d_{5/2}$ and Ba $3d_{3/2}$ at approximately 779.4 eV and 794.8 eV, respectively, indicative of Ba^{2+} ions. The Fe 2p spectra exhibited prominent peaks at 710.4–710.6 eV and 724.0 eV for Fe $2p_{3/2}$ and Fe $2p_{1/2}$, indicative of the Fe^{3+} state. Subsequent deconvolution confirmed the presence of Fe^{2+}. The O 1s spectra of the composites exhibited an asymmetric peak at approximately 529.7 eV, indicative of lattice oxygen in Bi–O bonds, and a shoulder peak at around 531.3 eV, suggestive of hydroxyl groups or adsorbed water. In the case of the electrodeposition samples, the presence of a peak at 532.8 eV may be indicative of exposure to moisture or residual organic species. The XPS results corroborate the successful synthesis of the composites.

3.2. Study of degradation and mineralization of organic pollutants

In this study, TC was selected as a model pollutant to assess the photocatalytic degradation and mineralization capabilities of BiOI-based materials in the presence of PMS. The form of TC can vary depending on the pH, given that its functional groups are susceptible to ionization. Accordingly, the study solution was adjusted to a pH of 7, which is typical for the majority of water bodies targeted for treatment. The stability of the TC solution at pH 7 was examined over a 60-day period in the absence of light and in a stagnant state. As shown in Fig. S3, the solution's absorbance demonstrated minimal variation over the course of the study. However, mineralization levels remained largely constant throughout the 60-day period, indicating that only a minor proportion of TC was mineralized. This limited mineralization is a cause for concern with regard to environmental and aquatic health, as it implies the presence of persistent pollutants in the water.

Prior to evaluating the performance of the photocatalysts, a series of preliminary tests were conducted to examine the impact of visible light irradiation, the presence of PMS, and their combination on the degradation and mineralization of TC. The objective of these experiments was to isolate the contributions of each factor to the overall process, thereby elucidating the specific impact of each variable on the observed outcomes. As illustrated in Fig. S4, the degradation and mineralization of TC were affected by these conditions, although the observed changes were not statistically significant. The extent of degradation did not exceed 20%, and the degree of mineralization remained below 4.2 ± 0.3%. Of three conditions tested, the combination of PMS and light had the most substantial effect. Following a 90-min period, the degradation values were found to be approximately 10.6 ± 0.8% for light, 15.3 ± 0.6% for PMS, and 16.9 ± 0.7% for the combination of the two. Similarly, the mineralization values were similarly low, with 1.3 ± 0.4% for light, 2.5 ± 0.2% for PMS, and 3.8 ± 0.3% for the combination.

The catalytic activity of the BiOI-based materials was examined under a variety of conditions, including exposure to light, PMS, and a combination of both. These studies demonstrated a decline in

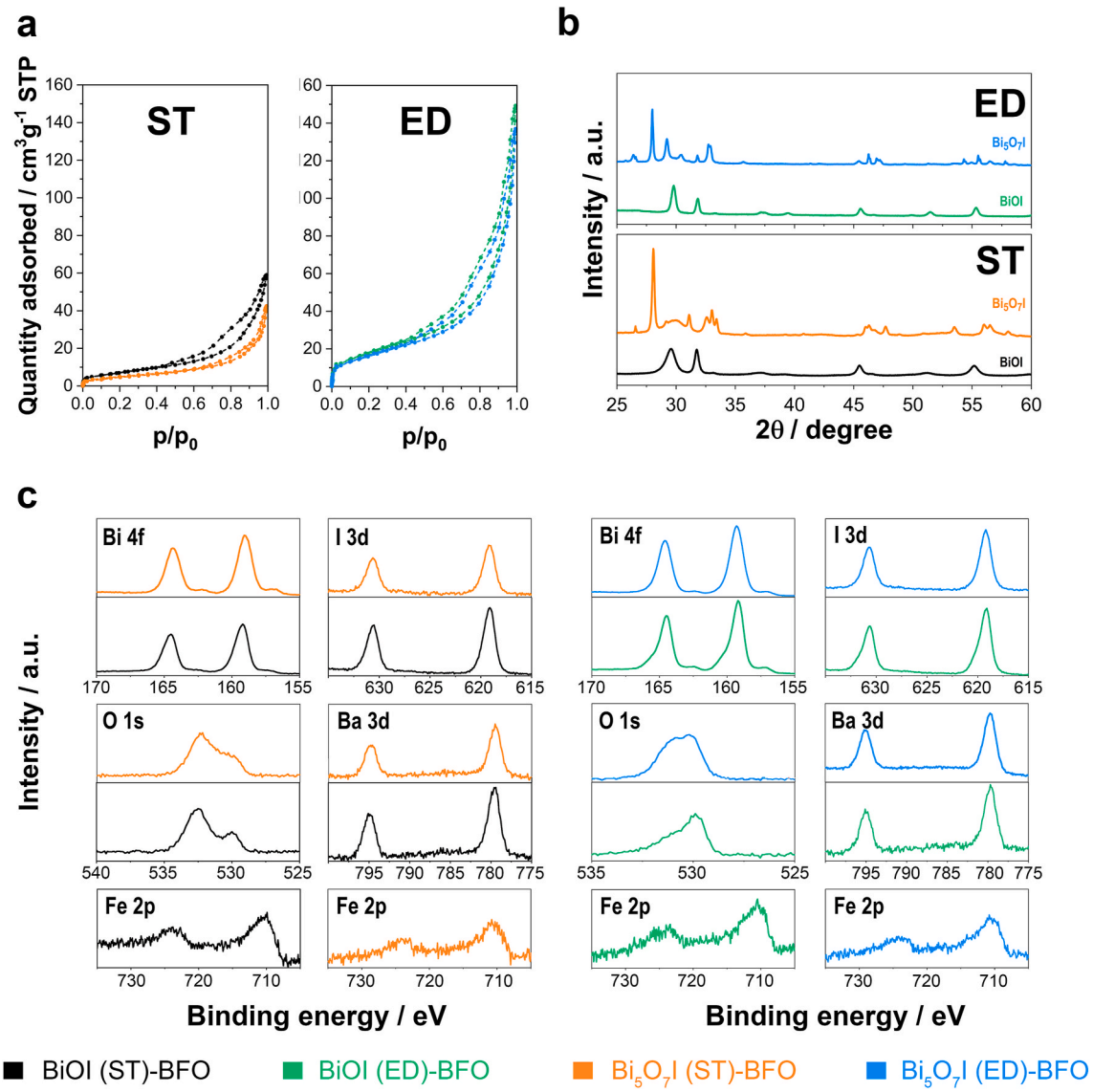

Fig. 4. Characterization of BiOI-based composites: (a) Nitrogen adsorption-desorption isotherms, (b) X-ray diffraction (XRD) patterns, and (c) X-ray photoelectron spectroscopy (XPS) spectra for Bi 4f, I 3d, O 1s, Ba 3d, and Fe 2p.

absorbance over time, indicative of progressive TC degradation. The findings substantiated that BiOI, in its diverse forms, demonstrated efficacy in the degradation and mineralization of TC in solution. The most pronounced degradation was observed when the solution was subjected to simultaneous exposure to light and PMS (Fig. 5).

Fig. 5a illustrates the degradation efficiencies of BiOI-based photocatalysts after 90 min under visible light irradiation, in the presence of PMS, and in combination, demonstrating distinct performance trends. In the presence of visible light, the BiOI (ST) and BiOI (ED) samples exhibited degradation efficiencies of 51.1 ± 0.5% and 59.1 ± 0.5%, respectively. The Bi_5O_7I (ST) sample exhibited an improvement in efficiency, reaching 40.4 ± 0.4%. In contrast, the Bi_5O_7I (ED) sample demonstrated a markedly higher efficiency, reaching 91.9 ± 0.6%. The formation of composites with $BaFe_{12}O_{19}$ resulted in a further enhancement in performance, with BiOI (ST)-BFO and BiOI (ED)-BFO reaching 75.3 ± 0.6% and 83.5 ± 0.4%, respectively. The Bi_5O_7I (ST)-BFO composite achieved a degradation efficiency of 66.4 ± 0.6%, which surpassed the performance of Bi_5O_7I (ST) alone. It is noteworthy that Bi_5O_7I (ED)-BFO exhibited the highest efficiency at 96.0 ± 0.7%, exceeding its performance under PMS.

In the presence of PMS, both BiOI (ST) and BiOI (ED) demonstrated superior performance, achieving degradation efficiencies of 61.0 ± 1.3% and 73.1 ± 0.7%, respectively. The efficiency of Bi_5O_7I (ST) was found to be the lowest at 18.10%, whereas that of Bi_5O_7I (ED) exhibited a marked improvement, reaching 79.3 ± 0.9%. The incorporation of BFO further augmented the performance of the system, with BiOI (ST)-BFO reaching 86.1 ± 0.9% and BiOI (ED)-BFO achieving 92.3 ± 1.0%. This represents the highest level of performance among the BiOI samples. The incorporation of BFO resulted in a notable enhancement in the overall efficiency of Bi_5O_7I, with the Bi_5O_7I (ST)-BFO reaching 73.4 ± 1.2% and the Bi_5O_7I (ED)-BFO achieving 94.8 ± 1.1%. This represents the highest overall efficiency observed in the presence of PMS over the specified time period.

In the presence of both visible light and PMS, electrodeposited BiOI-based photocatalysts demonstrated markedly superior performance compared to their solvothermal counterparts. The degradation rate achieved by BiOI (ED) was 64.2 ± 1.0%, which is approximately double that of BiOI (ST), which reached 36.8 ± 1.4%. Similarly, Bi_5O_7I (ED) demonstrated a substantially higher degradation rate of 74.9 ± 0.2% in comparison to Bi_5O_7I (ST), which exhibited a degradation rate of 24.1%. The incorporation of BFO further enhanced performance, with BiOI (ST)-BFO and Bi_5O_7I (ST)-BFO achieving 71.5 ± 0.2% and 54.9 ± 0.6%

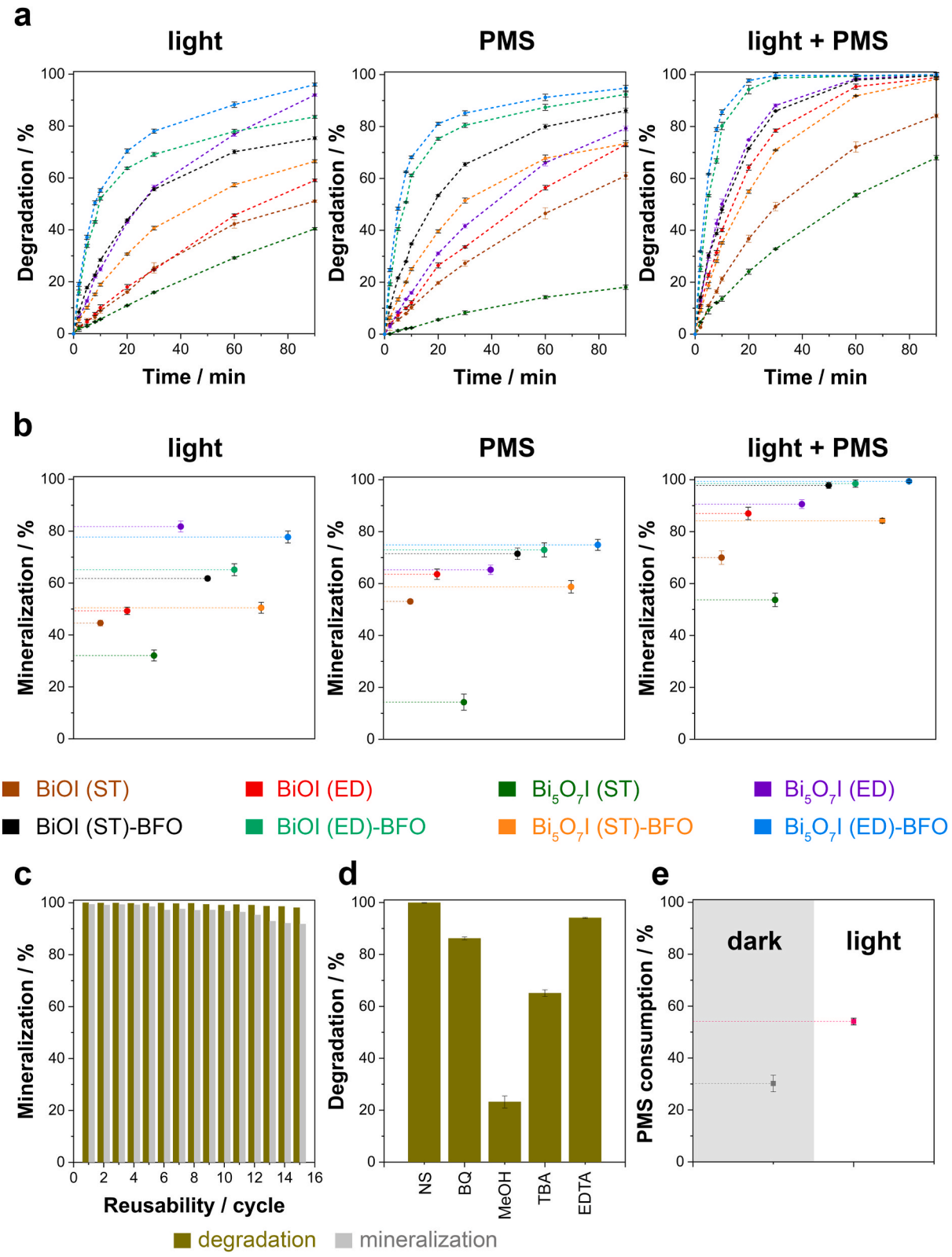

Fig. 5. (a) Degradation performance and (b) mineralization performance of BiOI-based catalysts under visible light irradiation (left), in the presence of PMS (center), and under the combination of visible light and PMS (right). (c) Degradation and mineralization of TC by Bi_5O_7I (ED)-BFO under the combination of visible light and PMS during 15 reusability cycles. (d) Trapping experiments with 1 mM of benzoquinone (BQ), 1 mM methanol (MeOH), 1 mM *tert*-butyl alcohol (TBA), or 1 mM ethylenediamine tetraacetic acid disodium salt (EDTA) after 90 min of visible light irradiation and in the presence of PMS. NS indicates experiments in the absence of scavengers. (e) PMS consumption in dark conditions and under visible light irradiation after 90 min. Experimental conditions: [TC] = 20 ppm, [PMS] = 2.5 mM, T = 25 °C, catalyst dosage = 0.5 mg mL^{-1}. All experiments were performed in triplicate.

degradation, respectively. It is noteworthy that BiOI (ED)-BFO and Bi_5O_7I (ED)-BFO achieved 94.2 ± 1.6% and 97.7 ± 0.6%, respectively, indicating a strong synergistic effect with BFO. Following a 90-min irradiation period, all photocatalysts exhibited markedly enhanced performance, with BiOI (ED) and Bi_5O_7I (ED) attaining near-complete degradation rates of 98.8% and 99.8 ± 0.4%, respectively. The incorporation of BFO once again proved advantageous, with BiOI (ST)-BFO and BiOI (ED)-BFO attaining 99.6 ± 0.4% and 99.8 ± 0.2%, respectively. Furthermore, Bi_5O_7I (ST)-BFO and Bi_5O_7I (ED)-BFO demonstrated high efficiencies, with the latter approaching complete degradation at 99.9 ± 0.1%. The observed consistency in performance enhancement with BFO incorporation indicates a notable increase in the number of available active sites for photocatalysis, which in turn results in superior overall degradation efficiency.

The analysis of mineralization values for TC solutions after 90 min under different conditions revealed notable variations in catalyst performance (Fig. 5b). In the presence of visible light, Bi_5O_7I (ED) exhibited the highest degree of mineralization, reaching 82 ± 2%. This makes it the most effective catalyst. In contrast, Bi_5O_7I (ST) had the lowest degree of mineralization at 32 ± 2%, indicating limited effectiveness. BFO composites, such as BiOI (ED)-BFO and Bi_5O_7I (ED)-BFO, exhibited improved mineralization compared to their non-composite counterparts, with values of 65.1 ± 2.3% and 78 ± 2%, respectively. This suggests that BFO enhances photocatalytic activity under visible light. When PMS was used alone, the observed trends underwent a shift. The BiOI (ED)-BFO composite achieved the highest mineralization, reaching 75 ± 2%. This highlights its superior performance with PMS. In contrast, Bi_5O_7I (ST) demonstrated minimal mineralization at 14 ± 3%, indicating limited effectiveness when used with PMS alone. In general, the use of PMS resulted in enhanced mineralization for the majority of catalysts, particularly those incorporating BFO composites. The combination of visible light and PMS universally yielded the highest mineralization values in all cases. Bi_5O_7I (ED)-BFO stood out with an impressive 99.4 ± 0.4% mineralization, nearly achieving complete TC mineralization. This combined approach underscores the enhanced catalytic activity facilitated by both visible light and PMS, with BFO composites significantly boosting the performance of BiOI and Bi_5O_7I catalysts across all conditions. Consequently, further studies focused on Bi_5O_7I (ED)-BFO, as it presented the most favourable degradation and mineralization rates.

The performance of Bi_5O_7I (ED)-BFO photocatalysts under visible light irradiation and in the presence of PMS was evaluated over 15 reuse cycles, with no treatment between cycles (Fig. 5c). The degradation efficiency commenced at 99.9% in the initial cycle and remained high, exhibiting a consistent range of 99.1%–99.9% from cycles 2 to 10. This indicates that the photocatalyst retains a notable capacity to degrade TC effectively, with minimal efficiency loss over multiple cycles. By the 15th cycle, a slight decline in degradation efficiency was observed, reaching 98.1%. This suggests that minor deactivation or fouling may have occurred due to the extended use. Nevertheless, the overall performance remains robust. In contrast, the mineralization efficiency commenced at 99.4% in the initial cycle and remained above 98% from cycles 2 to 5, indicating effective breakdown of TC into mineralized products. However, a notable decline in mineralization efficiency was observed from cycle 6 onwards, with values decreasing from 97.2% to 91.8% by the 15th cycle. This more pronounced decline in mineralization compared to degradation indicates that while the photocatalyst continues to break down TC molecules, its capacity to fully convert them into mineralized products diminishes more rapidly. This discrepancy may be attributed to the accumulation of intermediate degradation products on the catalyst surface or partial deactivation of active sites responsible for mineralization. Notwithstanding this decline, the Bi_5O_7I (ED)-BFO photocatalyst displays considerable activity, rendering it a promising candidate for repeated TC degradation applications. The implementation of strategies to mitigate the decrease in mineralization efficiency would serve to enhance its long-term effectiveness. However, the morphology and architecture of the catalysts remained unaltered throughout the 15 cycles of reuse. Furthermore, the amount of photocatalyst dissolved during these 15 cycles was less than 0.3%, with no iron ions detected in the solution.

To elucidate the photocatalytic mechanism of Bi_5O_7I (ED)-BFO during the degradation of TC, radical trapping experiments were conducted (Fig. 5d). This was accomplished by employing specific scavengers to identify various reactive species. The degradation efficiency was evaluated in the presence of these scavengers to ascertain the role of different radicals in the process. The absence of a scavenger resulted in a degradation efficiency of 99.9 ± 0.1%. The introduction of BQ to quench superoxide radicals ($O_2^{\bullet-}$) resulted in a notable decline in degradation efficiency, reaching 86.2 ± 0.6%. This observation indicates that superoxide radicals play a pivotal role, although they were not the most dominant. The introduction of methanol, which quenches both hydroxyl (·OH) and sulfate ($SO_4^{\bullet-}$) radicals, resulted in a significant decline in efficiency, with an efficiency remaining of 23 ± 2%. This underscores the pivotal role of these radicals in the degradation process. The introduction of TBA, which specifically quenches hydroxyl radicals, resulted in a notable reduction in efficiency, reaching 65 ± 1%. This observation underscores the substantial impact of hydroxyl radicals while also indicating the involvement of sulfate radicals, given the comparatively less pronounced decline in efficiency compared to MeOH. The introduction of EDTA, which targets holes (h^+), resulted in a slight reduction to 94.1 ± 0.2%. This finding indicates that holes contributed to the process but were not the primary reactive species (Gómez et al., 2023; Lai et al., 2018; Xu et al., 2016). In conclusion, the results demonstrate that hydroxyl and sulfate radicals were the primary drivers of the photocatalytic activated degradation of TC by Bi_5O_7I (ED)-BFO in the presence of PMS. Superoxide radicals and holes also played a significant but lesser role. This detailed understanding of the reactive species involved can inform strategies to optimize photocatalyst performance, enhancing the generation and activity of the key radicals for more efficient degradation processes.

The reduction in PMS concentration, indicative of sulfate radical formation, was investigated using Bi_5O_7I (ED)-BFO as the photocatalyst under both dark and visible light conditions (Fig. 5e). In the absence of light, the concentration of PMS was observed to decrease by 30 ± 3% after 90 min. This considerable reduction indicated that Bi_5O_7I (ED)-BFO was capable of activating PMS to a notable extent in the absence of light, resulting in the generation of sulfate radicals. This inherent catalytic activity indicates that the photocatalyst is capable of facilitating PMS decomposition in the absence of light. In contrast, visible light irradiation resulted in a notable increase in the reduction of PMS concentration, reaching 54 ± 1% after 90 min. This pronounced increase underscores the augmented photocatalytic activity of Bi_5O_7I (ED)-BFO when subjected to visible light. This enhancement was attributed to the activation of the photocatalyst's electronic states, which resulted in an increased generation of reactive radicals, including sulfate radicals. In comparison to the results obtained in the absence of light, the reduction in PMS concentration was found to be almost double that observed in the dark. These results clearly demonstrate the superior performance of Bi_5O_7I (ED)-BFO as a photocatalyst in light-assisted processes. The utilization of visible light markedly enhances the activation of PMS, promoting a higher rate of sulfate radical formation and, consequently, more effectively facilitating the degradation of contaminants.

To further elucidate the role of light in PMS activation by Bi_5O_7I (ED)-BFO and the subsequent generation of sulfate and hydroxyl radicals in the TC mineralization process, quantitative measurements were carried out using spectrophotometric methods (Fig. 6a and b). The relative concentration of sulfate radicals was indirectly determined by measuring the concentration of Ce(IV) using UV–Vis spectrophotometry, following the reaction between sulfate radicals and Ce(III) (Serrà et al., 2024). A calibration curve with known concentrations of Ce(IV) sulfate was employed to quantify the sulfate radicals. As illustrated in Fig. 6a, the concentration of Ce(IV), which correlates with sulfate radical

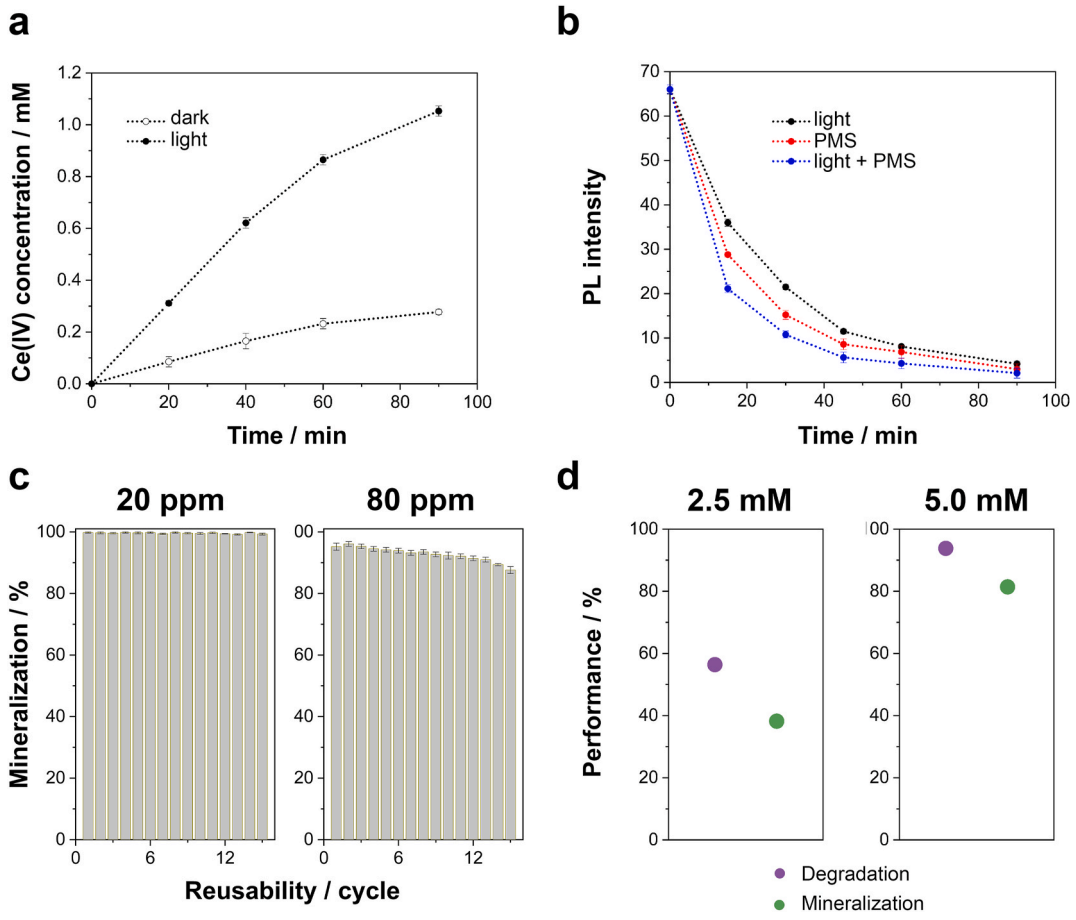

Fig. 6. (a) Concentration of Ce(IV) ions formed during the activation of 2.5 mM PMS using Bi_5O_7I (ED)-BFO in the dark and under visible light irradiation. (b) Time-dependent photoluminescence (PL) spectra of an 8 μM aqueous solution during the activation of 2.5 mM PMS using Bi_5O_7I (ED)-BFO in the dark and under visible light irradiation. Experimental conditions: [pollutant] = 0 ppm, [PMS] = 2.5 mM, T = 25 °C, catalyst dosage = 0.5 mg mL^{-1}. All experiments were conducted in triplicate. (c) Mineralization of multipollutant solution 1 (20 ppm, comprising 5 ppm each of TC, LEV, MB, and Rh–B) – left – and multipollutant solution 2 (80 ppm, comprising 20 ppm each of TC, LEV, MB, and Rh–B) – right – by Bi_5O_7I (ED)-BFO under visible light and PMS during 15 reusability cycles of 90 min (solution 1) and 180 min (solution 2). Experimental conditions: [pollutant] = 20 ppm (solution 1) or 80 ppm (solution 2), [PMS] = 2.5 mM (solution 1) or 10 mM (solution 2), T = 25 °C, catalyst dosage = 0.5 mg mL^{-1}. All experiments were conducted in triplicate. (d) Degradation of TC and mineralization of organic matter in tap water contaminated with 20 ppm of TC using Bi_5O_7I (ED)-BFO under visible light irradiation. Experimental conditions: [TC] = 20 ppm, [PMS] = 2.5 mM or 5.0 mM, T = 25 °C, catalyst dosage = 0.5 mg mL^{-1}. All experiments were conducted in triplicate.

generation, was approximately 3.8 times higher under light irradiation than in the dark. This result demonstrates a substantial increase in sulfate radical formation due to light exposure. It is noteworthy that after 90 min, PMS consumption reached 30% in the absence of light, while it was 54% under light irradiation. Although PMS consumption exhibited a mere 1.8-fold increase under illumination relative to the dark, sulfate radical generation demonstrated a 3.8-fold enhancement under the same conditions. This indicates that light irradiation primarily facilitates the radical-mediated decomposition of PMS, rather than non-radical pathways, which is essential for promoting the mineralization of organic pollutants.

Furthermore, the concentration of hydroxyl radicals was evaluated by monitoring the time-dependent decline in the fluorescence intensity of fluorescein sodium salt. Fig. 6b illustrates that the reduction in fluorescence, indicative of hydroxyl radical formation, was 1.4 times higher in the presence of PMS and 1.9 times higher when both PMS and light irradiation were applied. These findings, in conjunction with trapping experiments, substantiate the assertion that hydroxyl radicals were instrumental in the mineralization process of TC, with their formation markedly augmented in the presence of PMS and light. This reinforces the significance of both sulfate and hydroxyl radicals in facilitating efficacious pollutant degradation in light-assisted PMS activation.

Fig. 6c depicts the mineralization performance of Bi_5O_7I (ED)-BFO photocatalyst across a range of pollutant solutions, thereby offering insights into its efficacy and stability over multiple reusability cycles. In Solution 1, which contained a total of 20 ppm comprising 5 ppm each of TC, LEV, MB, and Rh–B, the photocatalyst exhibited consistent and exceptional mineralization rates exceeding 99% after 90 min of visible light exposure. Over 15 reusability cycles, the Bi_5O_7I (ED)-BFO photocatalyst demonstrated high mineralization efficiency (>99%), indicating its robust stability in degrading this mixture of organic pollutants under visible light. In contrast, multipollutant Solution 2, which had a higher total concentration of 80 ppm (20 ppm of each pollutant), demonstrated initial mineralization rates of 95.2% after 180 min, which subsequently declined to 87.6% after 15 cycles. This decline indicates that the higher initial pollutant concentration accelerated the deactivation of the catalyst over the course of multiple cycles, emphasizing the difficulty of maintaining consistent performance when faced with elevated pollutant concentrations. It is noteworthy that Solution 1 utilized 2.5 mM PMS, whereas Solution 2 employed 10 mM PMS. In comparison, the single-pollutant solution of 20 ppm TC demonstrated superior mineralization efficiency and enhanced stability over 15 cycles in comparison to multipollutant Solution 1. These findings suggest that while Bi_5O_7I (ED)-BFO was capable of effectively degrading multiple pollutants, elevated initial pollutant concentrations or a combination of diverse pollutant types may potentially impact its long-term

performance and stability. The extent of photocorrosion and catalyst dissolution during these cycles was minimal, with less than 0.9% of Bi_5O_7I (ED)-BFO dissolved. In conclusion, Bi_5O_7I (ED)-BFO displays considerable promise as a photocatalyst for the treatment of complex multipollutant solutions under visible light irradiation. Further research should focus on the optimization of catalyst design and operational conditions with a view to enhancing stability and efficiency, particularly in scenarios involving higher pollutant concentrations and diverse pollutant compositions. An understanding of the mechanisms of radical generation and pollutant degradation will be of paramount importance for the advancement of the practical applications of this photocatalyst in environmental remediation.

To illustrate the material's capacity to activate PMS in more intricate and authentic settings, the deterioration of TC and the mineralization of organic matter in a solution prepared with tap water and containing 20 ppm of added TC were examined. As illustrated in Fig. 6d, following the introduction of PMS at a concentration of 2.5 mM, the degradation efficiency exhibited a notable decline, from 99.9 ± 0.1% to 56.4 ± 0.3%, over the course of 90 min. With regard to mineralization, it should be noted that the tap water already contained 4.9 ppm of organic matter in addition to the 20 ppm of TC. After 90 min, the process achieved a mineralization rate of 38.2 ± 0.2%. These findings indicate that the complex matrix of tap water, which contains both organic and inorganic species, can significantly reduce the efficiency of degradation and mineralization. Prior research indicates that the presence of inorganic salts may exert either a positive or negative impact on the rate of degradation and mineralization of TC and other organic compounds. However, doubling the PMS concentration to 5 mM resulted in notable improvements, with degradation reaching 93.8 ± 0.1% and mineralization increasing to 81.4 ± 0.2%. These findings underscore the material's potential for maintaining effective performance in more challenging real-world conditions.

4. Conclusions

This study presents the successful synthesis and application of bismuth oxyiodide-based composites for the activation of PMS under visible light, with a particular focus on the degradation of pharmaceutical pollutant in aqueous environments. The key findings provide valuable insights into the efficacy and potential of these materials for environmental remediation applications. The synthesis methods, including solvothermal and electrodeposition, yielded disparate morphologies of BiOI and Bi_5O_7I, with their surface characteristics and crystalline structures being shaped by the synthesis and annealing processes. Solvothermal synthesis yielded regular microspheres of BiOI with well-defined nanosheets, while electrodeposition produced heterogeneous flower-like structures. Upon annealing, these were transformed into Bi_5O_7I exhibiting either compact or spongier morphologies, impacting their surface areas and crystalline structures. These structural variations directly impacted the photocatalytic efficiency, thereby underscoring the pivotal role of material design in optimizing performance for environmental applications.

The incorporation of barium ferrite ($BaFe_{12}O_{19}$, BFO) nanoparticles into the bismuth oxyiodide matrices resulted in a notable enhancement of their photocatalytic performance. This synergy between the bismuth oxyiodides and magnetic ferrites resulted in enhanced surface areas and catalytic efficiencies, as corroborated by SEM, XRD, and XPS analyses. The photocatalytic experiments demonstrated that Bi_5O_7I (ED)-BFO composites are highly effective in the degradation and mineralization of TC, achieving 99.8% degradation and 99.4% mineralization in just 90 min. These findings highlight the material's potential as a robust photocatalyst for real-world environmental remediation.

However, when the material was tested in tap water, which is a more complex and realistic matrix, the initial performance was reduced due to the presence of organic and inorganic species. Notwithstanding this challenge, a notable enhancement in both degradation and mineralization rates was observed with an increase in PMS concentration, indicating that these materials retain their efficacy under more demanding conditions. This capacity to adapt and sustain performance in less controlled settings underscores the practicality of these materials for real-world applications, particularly in industrial and municipal water treatment systems where water quality is variable.

In addition to these technical contributions, this research offers broader implications for environmental sustainability. The combination of visible-light activation and PMS-based advanced oxidation processes with bismuth oxyiodide composites provides a promising avenue for the development of cost-effective, scalable, and environmentally sustainable solutions for pollutant degradation. The durability and reusability demonstrated over multiple cycles further enhance the appeal of these materials for long-term deployment in water treatment facilities. It is conceivable that these materials could be extended to address a wider range of organic pollutants, extending beyond pharmaceuticals, in a variety of environmental contexts.

In the future, further research should be conducted with the aim of optimizing these composites for even greater catalytic efficiency in real-world water matrices. Furthermore, an investigation into the degradation mechanisms of a variety of pollutants, an understanding of the interactions between these materials and other waterborne substances, and an exploration of potential modifications to enhance selectivity and efficiency could open new avenues for these composites in global environmental remediation efforts. The encouraging outcomes of this investigation provide a foundation for the advancement of next-generation catalysts that could serve a pivotal role in addressing critical environmental challenges, thereby contributing to enhanced water quality and public health outcomes on a larger scale.

CRediT authorship contribution statement

Laura Huidobro: Investigation, Data curation, Conceptualization. **Anna Domingo:** Investigation, Data curation, Conceptualization. **Elvira Gómez:** Writing – review & editing, Visualization, Supervision, Resources, Project administration, Methodology, Investigation, Formal analysis, Data curation, Conceptualization. **Albert Serrà:** Writing – review & editing, Writing – original draft, Visualization, Validation, Supervision, Resources, Project administration, Methodology, Investigation, Funding acquisition, Formal analysis, Conceptualization.

Declaration of competing interest

Authors declare no conflict of interest.

Acknowledgements

Grant Project PID2020-115663 GB-C32 financed by MICIU/AEI/10.13039/501100011033. Authors thank the CCiT-UB for the use of their equipment.

Appendix A. Supplementary data

Supplementary data to this article can be found online at https://doi.org/10.1016/j.chemosphere.2024.143532.

Data availability

Data will be made available on request.

References

Arumugam, M., Natarajan, T.S., Saelee, T., Praserthdam, S., Ashokkumar, M., Praserthdam, P., 2021. Recent developments on bismuth oxyhalides (BiOX; X = Cl, Br, I) based ternary nanocomposite photocatalysts for environmental applications. Chemosphere 282, 131054. https://doi.org/10.1016/j.chemosphere.2021.131054.

Ashraf, G.A., Rasool, R.T., Fadhali, M.M., Al-Sulaimi, S., Saleem, M.F., Hassan, N., Ajmal, Z., Mahmood, S., Samia, Faiq saeed, Balakrishnan, D., Jeridi, M., Guo, H., 2024. Novel magnetic Carbon@$BaBiFe_{12}O_{19}$ photocatalyst for efficient pollutants degradation under peroxymonosulfate activation. Mater. Sci. Semicond. Process. 176, 108291. https://doi.org/10.1016/j.mssp.2024.108291.

Bayantong, A.R.B., Shih, Y.J., Dong, C. Di, Garcia-Segura, S., de Luna, M.D.G., 2021. Nickel ferrite nanoenabled graphene oxide ($NiFe_2O_4$@GO) as photoactive nanocomposites for water treatment. Environ. Sci. Pollut. Res. 28, 5472–5481. https://doi.org/10.1007/s11356-020-10545-1.

Bein, E., Yecheskel, Y., Zucker, I., Drewes, J.E., Hübner, U., 2023. A novel catalytic filtration process using MnO_2@sand and peroxymonosulfate for unselective removal of organic contaminants from water. Chem. Eng. J. 476, 146636. https://doi.org/10.1016/j.cej.2023.146636.

Brillas, E., 2022. Progress of homogeneous and heterogeneous electro-Fenton treatments of antibiotics in synthetic and real wastewaters. A critical review on the period 2017–2021. Sci. Total Environ. 819, 153102. https://doi.org/10.1016/j.scitotenv.2022.153102.

Bujaldón, R., Benamara, M., Dhahri, R., Gómez, E., Serrà, A., 2024. Attuning doped ZnO-based composites for an effective light-driven mineralization of pharmaceuticals via PMS activation. Chemosphere 357, 142127. https://doi.org/10.1016/j.chemosphere.2024.142127.

Cao, F., Yang, L., Zhang, Y., Zhao, X., Lu, H., Wang, J., 2022. Peroxymonosulfate activation in ultrasound-driven molybdenum disulfide piezocatalysis: the effect of sulfur vacancy. J. Clean. Prod. 380, 135002. https://doi.org/10.1016/j.jclepro.2022.135002.

Felisardo, R.J.A., Brillas, E., Romanholo Ferreira, L.F., Cavalcanti, E.B., Garcia-Segura, S., 2023. Degradation of the antibiotic ciprofloxacin in urine by electrochemical oxidation with a DSA anode. Chemosphere 344, 140407. https://doi.org/10.1016/j.chemosphere.2023.140407.

Gómez, E., Fons, A., Cestaro, R., Serrà, A., 2023. Enhanced activation of peroxymonosulfate for tetracycline degradation using CoNi-based electrodeposited films. Nanomaterials 13 (5), 790. https://doi.org/10.3390/nano13050790.

Guo, S., Wang, H., Yang, W., Fida, H., You, L., Zhou, K., 2020. Scalable synthesis of Ca-doped α-Fe_2O_3 with abundant oxygen vacancies for enhanced degradation of organic pollutants through peroxymonosulfate activation. Appl. Catal. B Environ. 262, 118250. https://doi.org/10.1016/j.apcatb.2019.118250.

Hjiri, M., Bujaldón, R., Lloreda, J., Gómez, E., Serrà, A., 2024. Advanced degradation of organic pollutants using sonophotocatalytic peroxymonosulfate activation with $CoFe_2O_4$/Cu- and Ce-doped SnO_2 composites. Chemosphere 354, 141656. https://doi.org/10.1016/j.chemosphere.2024.141656.

Hu, J., Weng, S., Zheng, Z., Pei, Z., Huang, M., Liu, P., 2014. Solvents mediated-synthesis of BiOI photocatalysts with tunable morphologies and their visible-light driven photocatalytic performances in removing of arsenic from water. J. Hazard Mater. 264, 293–302. https://doi.org/10.1016/j.jhazmat.2013.11.027.

Huidobro, L., Bautista, Q., Alinezhadfar, M., Gómez, E., Serrà, A., 2024. Enhanced visible-light-driven peroxymonosulfate activation for antibiotic mineralization using electrosynthesized nanostructured bismuth oxyiodides thin films. J. Environ. Chem. Eng. 12, 112545. https://doi.org/10.1016/j.jece.2024.112545.

Kanakaraju, D., Glass, B.D., Oelgemöller, M., 2018. Advanced oxidation process-mediated removal of pharmaceuticals from water: a review. J. Environ. Manag. 219, 189–207. https://doi.org/10.1016/j.jenvman.2018.04.103.

Lai, L., Yan, J., Li, J., Lai, B., 2018. Co/Al_2O_3-EPM as peroxymonosulfate activator for sulfamethoxazole removal: performance, biotoxicity, degradation pathways and mechanism. Chem. Eng. J. 343, 676–688. https://doi.org/10.1016/j.cej.2018.01.035.

Lee, S., Park, Y., Pradhan, D., Sohn, Y., 2016. AgX (X = Cl, Br, I)/BiOX nanoplates and microspheres for pure and mixed (methyl orange, rhodamine B and methylene blue) dyes. J. Ind. Eng. Chem. 35, 231–252. https://doi.org/10.1016/j.jiec.2015.12.040.

Li, Z., Feng, L., Zhang, L., Gao, P., Liu, Y., 2024. Fabrication of porous and defect-rich BiOI/MWCNTs photocatalyst by Ar plasma-etching for emerging pollutants degradation. Environ. Res. 252, 119015. https://doi.org/10.1016/j.envres.2024.119015.

Lim, J., Hoffmann, M.R., 2020. Peroxymonosulfate (PMS) activation on cobalt-doped TiO_2 nanotubes: degradation of organics under dark and solar light irradiation conditions. Environ. Sci.: Nano 7, 1602–1611. https://doi.org/10.1039/d0en00131g.

Lima, N.S., Souza, É.M., Torres, N.H., Bergamasco, R., Marques, M.N., Garcia-Segura, S., Sanchez de Alsina, O.L., Cavalcanti, E.B., 2019. Relevance of adjuvants and additives of pesticide commercial formulation on the removal performance of glyphosate by electrochemically driven processes. J. Clean. Prod. 212, 837–846. https://doi.org/10.1016/j.jclepro.2018.12.007.

Liu, C., Wang, X.J., 2016. Room temperature synthesis of $Bi_4O_5I_2$ and Bi_5O_7I ultrathin nanosheets with a high visible light photocatalytic performance. Dalton Trans. 45, 7720–7727. https://doi.org/10.1039/c6dt00530f.

Lv, W., Cao, H., Guan, Y., Wu, M., Liu, H., Guo, X., Yao, T., Chen, P., Sheng, L., Wu, J., 2024. Mediating peroxymonosulfate activation path in Fenton-like reaction via doping different metal atoms into g-C_3N5. J. Colloid Interface Sci. 674, 416–427. https://doi.org/10.1016/j.jcis.2024.06.160.

Matiur, R.M.D., Abuelwafa, A.A., Kato, S., Kishi, N., Soga, T., 2021a. A comparative study on optical properties of BiOI, $Bi_7O_9I_3$ and Bi_5O_7I materials. Opt. Mater. 111, 110677. https://doi.org/10.1016/j.optmat.2020.110677.

Matiur, R. Md, Abuelwafa, A.A., Putri, A.A., Kato, S., Kishi, N., Soga, T., 2021b. Annealing effects on structural and photovoltaic properties of the dip-SILAR-prepared bismuth oxyhalides (BiOI, $Bi_7O_9I_3$, Bi_5O_7I) films. SN Appl. Sci. 3, 1–11. https://doi.org/10.1007/s42452-021-04153-y.

Meng, D., Zhang, G., Li, S., Yang, F., 2024. Photoelectrochemical intensified efficient phosphorus recovery from hypophosphite and sulfadiazine co-contaminated wastewater by blue TiO_2 nanotube arrays anode. Sep. Purif. Technol. 351, 128032. https://doi.org/10.1016/j.seppur.2024.128032.

Mera, A.C., Rodríguez, C.A., Meléndrez, M.F., Valdés, H., 2017. Synthesis and characterization of BiOI microspheres under standardized conditions. J. Mater. Sci. 52, 944–954. https://doi.org/10.1007/s10853-016-0390-x.

Miklos, D.B., Remy, C., Jekel, M., Linden, K.G., Drewes, J.E., Hübner, U., 2018. Evaluation of advanced oxidation processes for water and wastewater treatment – a critical review. Water Res. 139, 118–131. https://doi.org/10.1016/j.watres.2018.03.042.

Pang, Y., Zhou, J., Yang, X., Lan, Y., Chen, C., 2021. Rationally designed Co_3O_4-SnO_2 activated peroxymonosulfate for the elimination of chloramphenicol. Chem. Eng. J. 418, 129401. https://doi.org/10.1016/j.cej.2021.129401.

Paragas, L.K.B., Dien Dang, V., Sahu, R.S., Garcia-Segura, S., de Luna, M.D.G., Pimentel, J.A.I., Doong, R.-A., 2021. Enhanced visible-light-driven photocatalytic degradation of acetaminophen over CeO_2/I, K-codoped C_3N_4 heterojunction with tunable properties in simulated water matrix. Sep. Purif. Technol. 272, 117567. https://doi.org/10.1016/j.seppur.2020.117567.

Putri, A.A., Kato, S., Kishi, N., Soga, T., 2019. Study of annealing temperature effect on the photovoltaic performance of BiOI-based materials. Appl. Sci. 9 (16), 3342. https://doi.org/10.3390/app9163342.

Qi, C., Liu, X., Ma, J., Lin, C., Li, X., Zhang, H., 2016. Activation of peroxymonosulfate by base: implications for the degradation of organic pollutants. Chemosphere 151, 280–288. https://doi.org/10.1016/j.chemosphere.2016.02.089.

Qin, X., Cheng, H., Wang, W., Huang, B., Zhang, X., Dai, Y., 2013. Three dimensional BiOX (X=Cl, Br and I) hierarchical architectures: Facile ionic liquid-assisted solvothermal synthesis and photocatalysis towards organic dye degradation. Mater. Lett. 100, 285–288. https://doi.org/10.1016/j.matlet.2013.03.045.

Roberts, S.C., Zembower, T.R., 2021. Global increases in antibiotic consumption: a concerning trend for WHO targets. Lancet Infect. Dis. 21, 10–11. https://doi.org/10.1016/S1473-3099(20)30456-4.

Robins, K., O'Donnell, G., Neumann, A., Schmidt, W., Hart, A., Graham, D.W., 2024. Antimicrobial resistance in rural rivers: comparative study of the Coquet (Northumberland) and eden (Cumbria) river catchments. Sci. Total Environ. 928, 172348. https://doi.org/10.1016/j.scitotenv.2024.172348.

Serrà, A., Gómez, E., al Hoda al Bast, N., Zhang, Y., Duque, M., José Esplandiu, M., Esteve, J., Nogués, J., Sepúlveda, B., 2024. Wireless pulsed nanophotoelectrochemical cell for the ultrafast degradation of organic pollutants. Chem. Eng. J. 487, 150663. https://doi.org/10.1016/j.cej.2024.150663.

Shang, J., Zhang, T., Li, X., Luo, Y., Feng, D., Cheng, X., 2023. Mn_3O_4-$ZnMn_2O_4$/SnO_2 nanocomposite activated peroxymonosulfate for efficient degradation of ciprofloxacin in water. Sep. Purif. Technol. 311, 123342. https://doi.org/10.1016/j.seppur.2023.123342.

Shi, X., Chen, Xiliang, Chen, Xin, Zhou, S., Lou, S., 2012. Solvothermal synthesis of BiOI hierarchical spheres with homogeneous sizes and their high photocatalytic performance. Mater. Lett. 68, 296–299. https://doi.org/10.1016/j.matlet.2011.10.063.

Tekin, G., Ersöz, G., Atalay, S., 2023. Comparison of synthesis methods for BiOI/g-C_3N_4 heterojunction photocatalysts and testing their visible light activity in sugar processing wastewater treatment. J. Ind. Eng. Chem. 126, 292–306. https://doi.org/10.1016/j.jiec.2023.06.020.

Wacławek, S., Lutze, H.V., Grübel, K., Padil, V.V.T., Černík, M., Dionysiou, D.D., 2017. Chemistry of persulfates in water and wastewater treatment: a review. Chem. Eng. J. 330, 44–62. https://doi.org/10.1016/j.cej.2017.07.132.

Wang, J., Li, B., Li, Y., Fan, X., Zhang, F., Zhang, G., Peng, W., 2021a. Facile synthesis of atomic Fe-N-C materials and dual roles investigation of Fe-N_4 sites in Fenton-like reactions. Adv. Sci. 8, 1–11. https://doi.org/10.1002/advs.202101824 aricle number: 2101824.

Wang, J., Wang, S., 2020. Reactive species in advanced oxidation processes: formation, identification and reaction mechanism. Chem. Eng. J. 401, 126158. https://doi.org/10.1016/j.cej.2020.126158.

Wang, J., Wang, S., 2018. Activation of persulfate (PS) and peroxymonosulfate (PMS) and application for the degradation of emerging contaminants. Chem. Eng. J. 334, 1502–1517. https://doi.org/10.1016/j.cej.2017.11.059.

Wang, L., Wang, Liang, Du, Y., Xu, X., Dou, S.X., 2021b. Progress and perspectives of bismuth oxyhalides in catalytic applications. Mater. Today Phys. 16, 100294. https://doi.org/10.1016/j.mtphys.2020.100294.

Wang, Y., Deng, K., Zhang, L., 2011. Visible light photocatalysis of BiOI and its photocatalytic activity enhancement by in situ ionic liquid modification. J. Phys. Chem. C 115, 14300–14308. https://doi.org/10.1021/jp2042069.

Wang, Z., Liu, W., Jin, H., Ma, L., Gu, Q., Liu, X., 2024. Layered double hydroxide helps $LaFeO_3$ photocatalyst activate peroxymonosulfate to efficiently degrade dyes. Sep. Purif. Technol. 341, 126832. https://doi.org/10.1016/j.seppur.2024.126832.

Xia, J., Yin, S., Li, H., Xu, H., Xu, L., Zhang, Q., 2011a. Enhanced photocatalytic activity of bismuth oxyiodine (BiOI) porous microspheres synthesized via reactable ionic liquid-assisted solvothermal method. Colloids Surfaces A Physicochem. Eng. Asp. 387, 23–28. https://doi.org/10.1016/j.colsurfa.2011.07.023.

Xia, J., Yin, S., Li, H., Xu, H., Yan, Y., Zhang, Q., 2011b. Self-assembly and enhanced photocatalytic properties of BiOI hollow microspheres via a reactable ionic liquid. Langmuir 27, 1200–1206. https://doi.org/10.1021/la104054r.

Xu, Y., Ai, J., Zhang, H., 2016. The mechanism of degradation of bisphenol A using the magnetically separable $CuFe_2O_4$/peroxymonosulfate heterogeneous oxidation process. J. Hazard Mater. 309, 87–96. https://doi.org/10.1016/j.jhazmat.2016.01.023.

Xu, Y., Ge, F., Xie, M., Huang, S., Qian, J., Wang, H., He, M., Xu, H., Li, H., 2019. Fabrication of magnetic $BaFe_{12}O_{19}/Ag_3PO_4$ composites with an: in situ photo-Fenton-like reaction for enhancing reactive oxygen species under visible light irradiation. Catal. Sci. Technol. 9, 2563–2570. https://doi.org/10.1039/c8cy02449a.

Yuan, Q., Qu, S., Li, R., Huo, Z.Y., Gao, Y., Luo, Y., 2023. Degradation of antibiotics by electrochemical advanced oxidation processes (EAOPs): performance, mechanisms, and perspectives. Sci. Total Environ. 856, 159092. https://doi.org/10.1016/j.scitotenv.2022.159092.

Zhang, S., Xu, Z., Ji, T., Guan, P., Weng, Y., 2024. Carbon quantum dots modified MoS_2 for high-efficiency and long-endurance persulfate activation: enhanced electron transfer and piezoelectricity. Sep. Purif. Technol. 353, 128148. https://doi.org/10.1016/j.seppur.2024.128148.